A 2.5D micromagnetic solver for randomly distributed magnetic thin objects

A 2.5D micromagnetic solver for randomly distributed magnetic thin objects

Alessandra Manzin[a] and Riccardo Ferrero[a,b]

[a]*Istituto Nazionale di Ricerca Metrologica (INRIM), Strada delle Cacce 91, 10135 Torino, Italy*

[b]*Politecnico di Torino, Corso Duca degli Abruzzi 24, 10129 Torino, Italy*

Corresponding author:

Alessandra Manzin

Istituto Nazionale di Ricerca Metrologica

Strada delle Cacce 91

10135 Torino, Italy

tel. +39-011-3919825

e-mail: a.manzin@inrim.it

Abstract

This paper presents a GPU-parallelized 2.5D micromagnetic solver for the efficient calculation of the magnetization configuration and hysteresis loop of 3D random distributions of magnetic thin-film objects, strongly interacting in the space. To well-reproduce complex shapes, the exchange field is calculated with a finite difference approach able to handle non-structured meshes. To enable the treatment of many objects, the magnetostatic field is locally separated into two contributions: an internal and an external one. The first term includes the magnetostatic interactions internal to each object and is obtained by numerically solving the Green's integral equation. The second term describes the inter-object magnetostatic interactions and it is determined by approximating each object as a collection of magnetic dipoles, associated with mesh elements. The accuracy and computational efficiency of the solver are analysed by comparison to a standard 3D-FFT code and to a reference code, where all the magnetostatic field terms are evaluated by numerically solving the Green's integral equation.

Keywords: Micromagnetics; Landau-Lifshitz-Gilbert equation; Magnetostatic interaction; GPU computing; Numerical modelling.

1. Introduction

In the last two decades, a lot of efforts have been made to speed-up micromagnetic simulations, with the aim of efficiently modelling the magnetization evolution in samples with large size, i.e. higher than some microns. One of the main critical aspects regards the spatial integration of the Landau-Lifshitz-Gilbert (LLG) equation, since this task involves the calculation of both short-range and long-range interactions, corresponding to the exchange and magnetostatic fields, respectively. To guarantee an accurate prediction of magnetization configuration, we have to discretize the sample with a mesh, whose scale should be comparable with the material exchange length, typically in the order of 5-10 nm. On such fine mesh, the magnetostatic field integration becomes very demanding if we have to study magnetic objects with size larger than one micron. The reason is that with classical integration techniques the computation cost of this task is quantifiable in $O(N^2)$ operations, where N is the number of mesh elements.

Several strategies have been implemented to make more efficient the calculation of the magnetostatic field, like Fast-Multipole methods [1-7], Fast Fourier Transform (FFT) techniques [8, 9] and hybrid approaches combing FFT and multipole expansion [10, 11]. To accurately handle curved structures, finite-element solvers have also been developed, integrating the Poisson equation by means of Finite Element Method (FEM) [12-14] or hybrid approaches that couple FEM with open boundary techniques, like the Boundary Element Method (BEM) [15, 16]. Finally, particular attention has been paid to the development of parallelized micromagnetic solvers, which exploit massively parallel architectures based on multiprocessor systems and, more recently, on graphical processing units (GPUs) [8, 17-23].

The spatial integration of the LLG equation becomes even more critical when a high number of interacting objects has to be simulated, since both large memory consumption and long computation time are required. As examples, this problem can be encountered when modelling large dot/antidot arrays for magnetic storage, magneto-logic devices or magnetic field sensors [24-27], artificial spin-ice structures [28] and magnetic nanomaterials for biomedical applications, like magnetic hyperthermia [29-31]. In the last example, the nano-objects can be randomly distributed in a three-dimensional (3D) space (a biological fluid or a tissue) at locally elevated concentrations and with very different orientations with respect to the applied field. In this case, 3D-FFT techniques, typically employed for the calculation of the magnetostatic field, cannot be applied, since they require structured meshes, which are not suitable for samples with complex shape and orientation not-aligned with the mesh grid. In particular, the use of structured meshes can lead to large inaccuracies when trying to model objects with strong shape anisotropy, e.g. thin-film samples. For this specific case, also 3D FEM is not suitable, since strongly irregular mesh elements should be employed to

simultaneously discretize the ensemble of thin objects and the 3D medium where they are randomly distributed. Moreover, the solution accuracy and computational cost strongly depend on the size of the domain selected for approximating the open boundary problem and on the order of the asymptotic boundary conditions, if applied [16]. As a possible solution, we could combine two-dimensional (2D) FEM, for the discretization of the thin objects, with BEM, for the treatment of the surrounding non-magnetic medium. However, the use of BEM leads to dense matrices and results in an additional computational complexity in the order of $O(M^2)$, where M is the number of boundary nodes.

In order to face with the above numerical problems, we have developed a two-and-a-half-dimensional (2.5D) GPU-parallelized micromagnetic solver, able to simulate a high number of interacting 2D-like nano-objects, randomly distributed in a not-meshed 3D space. Each nano-object is discretized with a non-structured mesh made of hexahedral elements, to well-reproduce complex shapes and very different mutual orientations. The exchange field is calculated with a finite difference technique able to handle non-structured meshes [32, 33], while the magnetostatic field is locally separated into two contributions: an internal and an external one. The internal term includes the interactions between magnetic spins in the hexahedra belonging to the same object. This is obtained by numerically solving the integral equation derived from Green's theorem application. The external term describes the inter-object magnetostatic interactions and it is determined by approximating the contribution from each mesh element as the stray field produced by a magnetic dipole [34, 35]. The time integration is performed by means of a norm-conserving scheme based on the Cayley transform and on the forward Euler method [36, 37]; this scheme has been proven to be very efficient in the determination of the equilibrium states along hysteresis loops [38].

We investigate the performances of the developed 2.5D micromagnetic solver, by analysing the accuracy in the calculation of the external magnetostatic contribution and the computation cost per each time instant. The solver is validated by comparison to a reference code, where all the magnetostatic field terms are evaluated by numerically solving the Green's integral equation, as well as to a standard 3D-FFT code. As a final goal, we demonstrate the solver reliability by calculating the hysteresis loop of a high number of magnetic nanodots, strongly interacting and randomly oriented in the space.

2. Methodology

We consider a set of N equal 2D-approximable magnetic bodies (flat objects with uniform very low thickness t) distributed in the 3D space. Each object is discretized with the same mesh composed of T hexahedra with height fixed to t (see Fig. 1). In each hexahedron the magnetization vector **M** is assumed to be uniform and its time evolution is determined under the hypothesis of no spatial

variation along t, by solving the Landau-Lifshitz-Gilbert (LLG) equation. For the generic i-th hexahedron belonging to the n-th object it results in

$$\frac{\partial \mathbf{M}_{i,n}}{\partial t} = -\frac{\gamma}{\left(1+\alpha^2\right)} \mathbf{M}_{i,n} \times \left[\mathbf{H}_{eff_{i,n}} + \frac{\alpha}{M_S} \left(\mathbf{M}_{i,n} \times \mathbf{H}_{eff_{i,n}} \right) \right], \; 1 \le i \le T, \; 1 \le n \le N \,, \tag{1}$$

where M_S is the saturation magnetization, γ is the absolute value of the gyromagnetic ratio and α is the damping coefficient. The effective field $\mathbf{H}_{eff}$ is the sum of the applied field $\mathbf{H}_a$, the exchange field $\mathbf{H}_{ex}$, the magnetocrystalline anisotropy field $\mathbf{H}_{an}$ and the magnetostatic field $\mathbf{H}_m$, which is in turn decomposed into an "internal" and an "external" term (Fig. 1). The internal term includes the magnetostatic contributions in the hexahedron of calculus due to the magnetic spins in all the other hexahedra belonging to the same object, namely

$$\mathbf{H}_{m,int_{i,n}} = \frac{1}{4\pi} \sum_{j=1, j\neq i}^{T} \int_{\partial\Omega_j} \mathbf{M}_{j,n} \cdot \mathbf{n}_j \frac{\left(\mathbf{r}_{i,n} - \mathbf{r}_{j,n} \right)}{\left\| \mathbf{r}_{i,n} - \mathbf{r}_{j,n} \right\|^3} ds, \; 1 \le i \le T, \; 1 \le n \le N \,, \tag{2}$$

where $\partial\Omega_j$ is the surface of the j-th hexahedron and $\mathbf{n}_j$ its normal unit vector, while $\mathbf{r}_{i,n}$ and $\mathbf{r}_{j,n}$ are the position vectors of the barycentres of the i-th and j-th hexahedra of the n-th object, respectively.

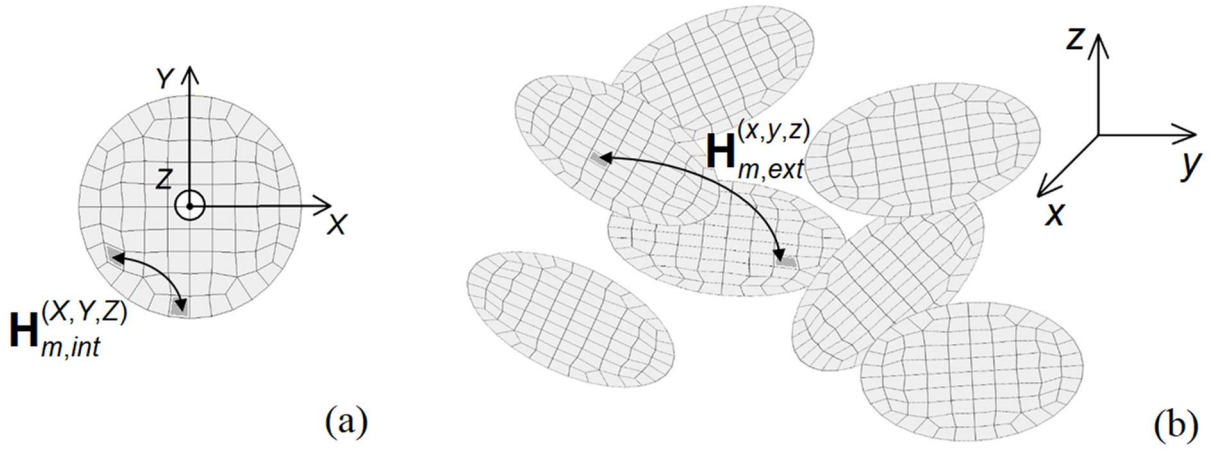

Fig. 1. (a) Schematic of the hexahedral mesh of a single object in coordinate system (X, Y, Z) (local reference frame) and representation of the interaction concurring to the internal magnetostatic field term. (b) Schematic of a 3D distribution of objects randomly arranged in coordinate system (x, y, z) (absolute reference frame) and representation of the interaction concurring to the external magnetostatic field term.

The external term includes the magnetostatic contributions in the hexahedron of calculus due to the magnetic spins in the hexahedra belonging to all the other objects. This is approximated by associating each hexahedron with a magnetic dipole centred in its barycentre, namely

$$\mathbf{H}_{m,ext_{i,n}} = \frac{1}{4\pi} \sum_{q=1,q\neq n}^{N} \sum_{j=1}^{T} \frac{3\left[\mathbf{m}_{j,q} \cdot \left(\mathbf{r}_{i,n} - \mathbf{r}_{j,q}\right)\right]\left(\mathbf{r}_{i,n} - \mathbf{r}_{j,q}\right)}{\left\|\mathbf{r}_{i,n} - \mathbf{r}_{j,q}\right\|^5} - \frac{\mathbf{m}_{j,q}}{\left\|\mathbf{r}_{i,n} - \mathbf{r}_{j,q}\right\|^3},\ 1 \le i \le T,\ 1 \le n \le N, \tag{3}$$

where $\mathbf{m}_{j,q}$ is the magnetic moment in the j-th hexahedron of the q-th object, equal to $\mathbf{M}_{j,q}\Delta V_j$, where ΔV_j is the volume of the j-th hexahedron.

2.1. Implementation

The developed 2.5D micromagnetic solver is composed of two main blocks. The first block, at the beginning, is related to the input of the geometry, the discretization mesh of a single object and the physical properties of the problem (pre-processing phase), followed by the calculation of the time-invariant system matrices for the exchange and internal magnetostatic fields. The second block is associated with the determination of the effective field contributions and the update of the magnetization at each time instant.

The first block starts with the input of the hexahedral mesh of a single object Ω in the local reference frame, i.e. the coordinate system (X, Y, Z), centred in the object barycentre and with Z-axis perpendicular to the object surface (Fig. 1(a)). Then, a 3D distribution of N objects is randomly arranged in the absolute reference frame, i.e. the coordinate system (x, y, z) (Fig. 1(b)), providing for each object the translation vector components (ΔX_n, ΔY_n, ΔZ_n) and the rotation (Euler) angles (φ_n, θ_n, ψ_n) for the transformation from (X, Y, Z) to (x, y, z). It results in

$$\begin{bmatrix} x \\ y \\ z \end{bmatrix} = \mathbf{R}_{\varphi\theta\psi_n} \begin{bmatrix} X \\ Y \\ Z \end{bmatrix} + \begin{bmatrix} \Delta X_n \\ \Delta Y_n \\ \Delta Z_n \end{bmatrix},\ 1 \le n \le N, \tag{4}$$

where $\mathbf{R}_{\varphi\theta\psi_n}$ is the rotation matrix for the n-th object that is expressed in the Goldstein's notation

$$\mathbf{R}_{\varphi\theta\psi_n} = \begin{bmatrix} \cos(\psi_n)\cos(\varphi_n) - \cos(\theta_n)\sin(\varphi_n)\sin(\psi_n) & -\sin(\psi_n)\cos(\varphi_n) - \cos(\theta_n)\sin(\varphi_n)\cos(\psi_n) & \sin(\theta_n)\sin(\varphi_n) \\ \cos(\psi_n)\sin(\varphi_n) + \cos(\theta_n)\cos(\varphi_n)\sin(\psi_n) & -\sin(\psi_n)\sin(\varphi_n) + \cos(\theta_n)\cos(\varphi_n)\cos(\psi_n) & -\sin(\theta_n)\cos(\psi_n) \\ \sin(\theta_n)\sin(\psi_n) & \sin(\theta_n)\cos(\psi_n) & \cos(\theta_n) \end{bmatrix}. \tag{5}$$

After inputting the geometry, physical parameters (M_S, exchange constant k_{ex} and magnetocrystalline properties) and source conditions (spatial-temporal distribution of $\mathbf{H}_a$), we calculate the time-invariant matrices $\mathbf{G}$ and $\mathbf{K}$ for the determination, in the local reference frame (X, Y, Z), of the internal

magnetostatic and exchange fields, respectively. Matrices **G** and **K** are described later, in Subsection 2.2.

The second block of the solver involves the time integration of the LLG equation, which is performed by means of the Cayley transform and the forward Euler method [36]. At each time step, for each object, the magnetization at instant t_k is transformed from the absolute reference frame (x, y, z) to the local one (X, Y, Z). For the i-th hexahedron of the n-th object, it results in

$$\mathbf{M}_{i,n}^{(X,Y,Z)}\left(t_k\right)=\mathbf{R}_{\varphi\theta\psi_n}^{-1}\mathbf{M}_{i,n}^{(x,y,z)}\left(t_k\right),\ 1\le i\le T,\ 1\le n\le N\ . \tag{6}$$

Then, for each object, we first compute the internal term of the magnetostatic field and the exchange field in the local reference frame, by using the $3T\times3T$ system matrices **G** and **K** calculated at the beginning and the spatial distribution of the magnetization vector, expressed in the local reference frame. For the n-th object

$$\begin{cases}\mathbf{H}_{m,int_n}^{(X,Y,Z)}\left(t_k\right)=\mathbf{G}\mathbf{M}_n^{(X,Y,Z)}\left(t_k\right)\\ \mathbf{H}_{ex_n}^{(X,Y,Z)}\left(t_k\right)=\mathbf{K}\mathbf{M}_n^{(X,Y,Z)}\left(t_k\right)\end{cases},\ 1\le n\le N\ . \tag{7}$$

K is reduced to a matrix **K*** with size $T\times T$, since the relative geometric contribution is the same for each component.

Second, we transform the two fields from (X, Y, Z) to (x, y, z) by means of the rotation matrix, resulting in the following operations for the i-th hexahedron of the n-th object:

$$\begin{cases}\mathbf{H}_{m,int_{i,n}}^{(x,y,z)}\left(t_k\right)=\mathbf{R}_{\varphi\theta\psi_n}\mathbf{H}_{m,int_{i,n}}^{(X,Y,Z)}\left(t_k\right)\\ \mathbf{H}_{ex_{i,n}}^{(x,y,z)}\left(t_k\right)=\mathbf{R}_{\varphi\theta\psi_n}\mathbf{H}_{ex_{i,n}}^{(X,Y,Z)}\left(t_k\right)\end{cases},\ 1\le i\le T,\ 1\le n\le N\ . \tag{8}$$

Then, by implementing equation (3), we determine $\mathbf{H}_{m,ext}^{(x,y,z)}\left(t_k\right)$, i.e. the external term of the magnetostatic field in the absolute reference frame (x, y, z). If present, we also calculate in (x, y, z) the magnetocrystalline anisotropy field and, by means of the Langevin approach, the thermal field [39]. At the end, the effective field $\mathbf{H}_{eff}^{(x,y,z)}\left(t_k\right)$ is determined, by summing all the field contributions obtained in coordinate system (x, y, z).

Finally, we update the magnetization vector in (x, y, z) by means of a geometric time-integration scheme based on the Cayley transform, which has long been used in computational mechanics to implement exact rotations [37]. The Cayley transform, applied to the generic vector **v**, is given by

$$\mathrm{cay}\left(\mathbf{v}\right)=\left(\mathbf{I}+\mathrm{skew}\left[\mathbf{v}/2\right]\right)\left(\mathbf{I}-\mathrm{skew}\left[\mathbf{v}/2\right]\right)^{-1}, \tag{9}$$

where skew [**v**/2] is a skew symmetric 3×3 matrix defined as

$$\text{skew}\left[\mathbf{v}/2\right]=\frac{1}{2}\begin{pmatrix} 0 & -v_z & v_y \\ v_z & 0 & -v_x \\ -v_y & v_x & 0 \end{pmatrix}. \tag{10}$$

For a fixed time step Δt, the application of Cayley transform to the LLG equation (1) leads to

$$\mathbf{M}_{i,n}^{(x,y,z)}\left(t_{k+1}\right)=\text{cay}\left(\Delta t\boldsymbol{\omega}_{k_{i,n}}^{(x,y,z)}\right)\mathbf{M}_{i,n}^{(x,y,z)}\left(t_k\right),\ 1\le i\le T,\ 1\le n\le N, \tag{11}$$

where

$$\boldsymbol{\omega}_{k_{i,n}}^{(x,y,z)}=\mathbf{A}_{k_{i,n}}+\sigma\mathbf{M}_{i,n}^{(x,y,z)}\left(t_k\right) \tag{12}$$

for the forward Euler method (one-step update). In (12) σ is an arbitrary scalar function of **M**, here assumed to be constant in time and uniform in space with value in the order of γ [36, 38], and $\mathbf{A}_k$ is the generator at the k-th time instant, namely

$$\mathbf{A}_{k_{i,n}}=\frac{\gamma}{\left(1+\alpha^2\right)}\left[\mathbf{H}_{eff_{i,n}}^{(x,y,z)}\left(t_k\right)+\frac{\alpha}{M_S}\left(\mathbf{M}_{i,n}^{(x,y,z)}\left(t_k\right)\times\mathbf{H}_{eff_{i,n}}^{(x,y,z)}\left(t_k\right)\right)\right]. \tag{13}$$

2.2. System matrix for internal magnetostatic field

In this Subsection we describe the $3T\times3T$ system matrix **G** for the determination of the internal term of the magnetostatic field in the local reference frame (X, Y, Z), in accordance with (3). The geometric interaction between the generic i-th and j-th hexahedra in the reference object Ω leads to the following 3×3 symmetric sub-matrix of **G**

$$\mathbf{G}^{ij}=\begin{bmatrix} g_{XX}^{ij} & g_{XY}^{ij} & g_{XZ}^{ij} \\ g_{YX}^{ij} & g_{YY}^{ij} & g_{YZ}^{ij} \\ g_{ZX}^{ij} & g_{ZY}^{ij} & g_{ZZ}^{ij} \end{bmatrix}, \tag{14}$$

where

$$g_{pq}^{ij}=\frac{1}{4\pi}\int_{\partial\Omega_j} n_{q_j}\frac{\left(p_{i,n}-p_{j,n}\right)}{\left\|\mathbf{r}_i-\mathbf{r}_j\right\|^3}ds \tag{15}$$

for p and q equal to local system coordinates X, Y or Z. The numerical integration in (14) is performed by means of the Gaussian quadrature rules with 9 nodes.

2.3. System matrix for exchange field

In this Subsection we describe the $T \times T$ system matrix **K*** for the determination of the p-th component of the exchange field in the local reference frame (X, Y, Z) at instant t_k, defined as

$$H_{ex_p}^{(X,Y,Z)}\left(t_k\right) = k_{ex}\left[\frac{\partial^2 M_p^{(X,Y,Z)}\left(t_k\right)}{\partial X^2} + \frac{\partial^2 M_p^{(X,Y,Z)}\left(t_k\right)}{\partial Y^2}\right], \tag{16}$$

where $p = X$, Y or Z and the derivative of $M_p^{(X,Y,Z)}\left(t_k\right)$ with respect to Z is assumed equal to zero, due to the thin-film approximation.

The exchange field is here computed by means of a finite difference method suitable for non-structured meshes, thus allowing the accurate treatment of curved boundaries [32, 33]. Focusing on the X-Y plane, the formulation is derived by approximating the magnetization vector by a second-order Taylor series expansion around the point of calculus (X_0, Y_0), namely

$$\begin{aligned}\mathbf{M}^{(X,Y,Z)} = \mathbf{M}_0^{(X,Y,Z)} + h\frac{\partial \mathbf{M}_0^{(X,Y,Z)}}{\partial X} + l\frac{\partial \mathbf{M}_0^{(X,Y,Z)}}{\partial Y} + \frac{h^2}{2}\frac{\partial^2 \mathbf{M}_0^{(X,Y,Z)}}{\partial X^2} + \frac{l^2}{2}\frac{\partial^2 \mathbf{M}_0^{(X,Y,Z)}}{\partial Y^2} + \\ + hl\frac{\partial^2 \mathbf{M}_0^{(X,Y,Z)}}{\partial X \partial Y} + O\left(\Delta^3\right)\end{aligned}, \tag{17}$$

where $h = X - X_0$, $l = Y - Y_0$ and $\Delta = \sqrt{h^2 + l^2}$.

By associating the points of calculus with the hexahedron barycentres, the five unknown derivatives in (17) can be obtained by considering the contributions from S surrounding hexahedra, where S is here assumed ~8 to avoid ill-conditioning.

For hexahedra located at the object boundaries $\partial\Omega$, the boundary condition on **M**

$$\left.\frac{\partial \mathbf{M}_0^{(X,Y,Z)}}{\partial \mathbf{n}}\right|_{\partial\Omega} = 0 \tag{18}$$

is imposed by introducing fictitious points outside Ω, replicating the magnetization value.

The five unknown derivatives of **M** in the generic i-th hexahedron of the n-th object can be determined via the minimization of the following norm

$$\Im = \sum_{j=1}^{S}\left[\left(\mathbf{M}_{i,n}^{(X,Y,Z)}(t_k)-\mathbf{M}_{j,n}^{(X,Y,Z)}(t_k)+h_{ij}\frac{\partial\mathbf{M}_{i,n}^{(X,Y,Z)}(t_k)}{\partial X}+l_{ij}\frac{\partial\mathbf{M}_{i,n}^{(X,Y,Z)}(t_k)}{\partial Y}+\right.\right.$$
$$\left.\left.+\frac{h_{ij}^2}{2}\frac{\partial^2\mathbf{M}_{i,n}^{(X,Y,Z)}(t_k)}{\partial X^2}+\frac{l_{ij}^2}{2}\frac{\partial^2\mathbf{M}_{i,n}^{(X,Y,Z)}(t_k)}{\partial Y^2}+h_{ij}l_{ij}\frac{\partial^2\mathbf{M}_{i,n}^{(X,Y,Z)}(t_k)}{\partial X\partial Y}\right)\frac{1}{\Delta_{ij}^3}\right]^2,\ 1\le i\le T,\ 1\le n\le N, \tag{19}$$

where $h_{ij}=X_i-X_j$, $l_{ij}=Y_i-Y_j$ and $\Delta_{ij}=\sqrt{h_{ij}^2+l_{ij}^2}$.

From $\dfrac{\partial\Im}{\partial\Delta\mathbf{M}_{i,n}^{(X,Y,Z)}(t_k)}=0$, we derive a 5×5 algebraic system of equations for the generic *p*-component of **M**, i.e.

$$\mathbf{C}\Delta\mathbf{M}_{p_{i,n}}^{(X,Y,Z)}(t_k)=\mathbf{D},\ 1\le i\le T,\ 1\le n\le N, \tag{20}$$

where the transpose of vector $\Delta\mathbf{M}_{p_{i,n}}^{(X,Y,Z)}$ is equal to

$$\left[\frac{\partial M_{p_{i,n}}^{(X,Y,Z)}}{\partial X}\ \frac{\partial M_{p_{i,n}}^{(X,Y,Z)}}{\partial Y}\ \frac{\partial^2 M_{p_{i,n}}^{(X,Y,Z)}}{\partial X^2}\ \frac{\partial^2 M_{p_{i,n}}^{(X,Y,Z)}}{\partial Y^2}\ \frac{\partial^2 M_{p_{i,n}}^{(X,Y,Z)}}{\partial X\partial Y}\right].$$

In (20) the 5×5 matrix **C** depends on mesh geometry, being a function of the distances between the hexahedra barycentres, while the 5×1 vector **D** depends on both mesh geometry and magnetization values at time instant t_k. The elements of **C** and **D** are detailed in Ref. [32].

By combining (16) and (20) for all the hexahedra in the reference object Ω we can derive the $T\times T$ system matrix **K***.

3. Results and discussion

3.1. Analysis of accuracy

In the developed 2.5D micromagnetic solver, possible sources of inaccuracy are introduced in (3) when evaluating the external magnetostatic field term. This is caused by the approximation of the contribution from a single hexahedron as the stray field of a magnetic dipole, located at the hexahedron barycentre [34, 35].

We here investigate the loss of accuracy in the calculation of the inter-object magnetostatic interactions, by first considering a set of simple test cases with two interacting squared thin-films made of permalloy (saturation magnetization M_S of 860 kA/m, exchange constant k_{ex} of 13 pJ/m and negligible magnetocrystalline anisotropy). The features and main results of the analysed cases are illustrated in Fig. 2. The reported schematics depict the configuration of the magnetization, which is

assumed to be uniformly distributed, with the same spatial orientation in the two films. In cases #1 and #2 the films are located in the *xy*-plane with a side-side distance *d*; in cases #3 and #4 the films are piled up with a face-face distance *h*. In cases #1 and #3 the magnetization lies in the *xy*-plane; in cases #2 and #4 it is orientated orthogonally to the film plane. The two squared films have a side of 200 nm and a thickness of 15 nm and are discretized with a structured mesh whose size in the *xy*-plane is fixed to ~3.5 nm.

Figure 2 also reports the maps of the module of the reference external magnetostatic field term, calculated by setting parameters *d* and *h* at 10 nm. Moreover, it shows the maps of the relative error, which is determined in the following way

$$E(\mathbf{r}) = \frac{\left\| \mathbf{H}_{m,ext}(\mathbf{r}) - \mathbf{H}_{m,ext}^{ref}(\mathbf{r}) \right\|}{\left\| \mathbf{H}_{m,ext}^{ref}(\mathbf{r}) \right\|} \cdot 100 \,. \tag{21}$$

In (21) $\mathbf{H}_{m,ext}$ is determined as in (3) and $\mathbf{H}_{m,ext}^{ref}$ is the reference solution, which is obtained by using the same approach adopted for the evaluation of the internal magnetostatic field term, calculating Green integrals via Gaussian quadrature rules with 9 nodes.

The highest relative errors are found for cases #1 and #2 in proximity to the adjacent sides, where peak errors in the order of 12% and 16% are encountered for #1 and #2, respectively (see Figs. 2(a) and 2(b)). The relative errors strongly decay by moving from the film side, going down 1% for distances from the boundary higher than 40 nm. Moreover, the peak values reduce to about 1% by increasing parameter *d* to 50 nm. Maximum errors in the order of 4% are found for cases #3 and #4, when *h* = 10 nm (see Figs. 2(c) and 2(d)). They reduce to less than 1% when *h* = 50 nm.

As a second test, we compare the above solutions with the one obtained by approximating the external magnetostatic field term as the interaction between objects represented by a unique magnetic dipole, centred in the object barycentre. It results in

$$\mathbf{H}_{m,ext_{i,n}}^{dip} = \frac{1}{4\pi} \sum_{q=1, q\neq n}^{N} \frac{3\left[\tilde{\mathbf{m}}_q \cdot \left(\mathbf{r}_{i,n} - \tilde{\mathbf{r}}_q\right)\right]\left(\mathbf{r}_{i,n} - \tilde{\mathbf{r}}_q\right)}{\left\|\mathbf{r}_{i,n} - \tilde{\mathbf{r}}_q\right\|^5} - \frac{\tilde{\mathbf{m}}_q}{\left\|\mathbf{r}_{i,n} - \tilde{\mathbf{r}}_q\right\|^3}, \; 1 \le i \le T, \, 1 \le n \le N \,, \tag{22}$$

where $\tilde{\mathbf{m}}_q$ is the magnetic moment of the *q*-th object and $\tilde{\mathbf{r}}_q$ the vector position of its barycentre. As can be seen in Fig. 3(a) for case #1 and *d* = 10 nm, this strong approximation leads to a significant increase in the relative errors. In particular, they reach peak values in the order of 85% when *d* = 10 nm and 50% when *d* = 50 nm, for cases #1 and #2. Very critical issues arise for cases # 3 and #4, due to the appearance of quasi-singularities in proximity to the position of the magnetic dipole that

approximates the contribution of an object to external magnetostatic field term. When h = 10 nm, for points located within 20 nm from the object barycentre the error tends practically to infinite.

As a third test, we analyse how the error introduced in the evaluation of the external magnetostatic field propagates during the solution of the LLG equation in a specified time interval. To this aim, we calculate the time evolution of the magnetization after the application of a uniform dc magnetic field, with amplitude variable between zero and 100 kA/m. The reference solution is obtained by calculating the external magnetostatic field term via Green integral evaluation. The damping coefficient α is fixed to 0.1, the time step to 50 fs and parameter σ in (12) to zero.

First, we consider the geometrical configuration and the initial magnetization state of case #1, with d = 10 nm and the external field applied along negative x-axis (inset of Fig. 3(b)). Figure 3(b) shows the relative error in the average value of the x-component of the magnetization at the equilibrium state reached at the end of the time evolution, versus the applied field amplitude. The errors are reported for the solutions obtained by approximating the external magnetostatic field term as in (3) (each hexahedron contributes as a dipole) and as in (22) (each object contributes as a dipole). For H_a = 0, an error higher than 4% is found for the object-dipole approximation, while the hexahedron-dipole approximation implemented in the 2.5D code leads to an error of 0.5%. This decreases to 0.004% when H_a = 100 kA/m.

Second, we consider the geometrical configuration and the initial magnetization state of case #4, with h = 10 nm and the external field applied along negative z-axis (inset of Fig. 3(c)). In this case, the hexahedron-dipole approximation is responsible for an error of about 0.1%, while the object-dipole approximation does not guarantee the reaching of the equilibrium state, also for large external fields, due to the appearance of quasi-singularities. This is well depicted by Fig. 3(c), which reports the time evolution of the average value of the z-component of the magnetization when H_a = 100 kA/m, for the reference and the two approximated solutions. From the above analysis, it is clear that the object-dipole approximation is inadequate in the calculation of hysteresis loops, since in presence of very close objects it introduces such strong errors to not permit the reaching of equilibrium states.

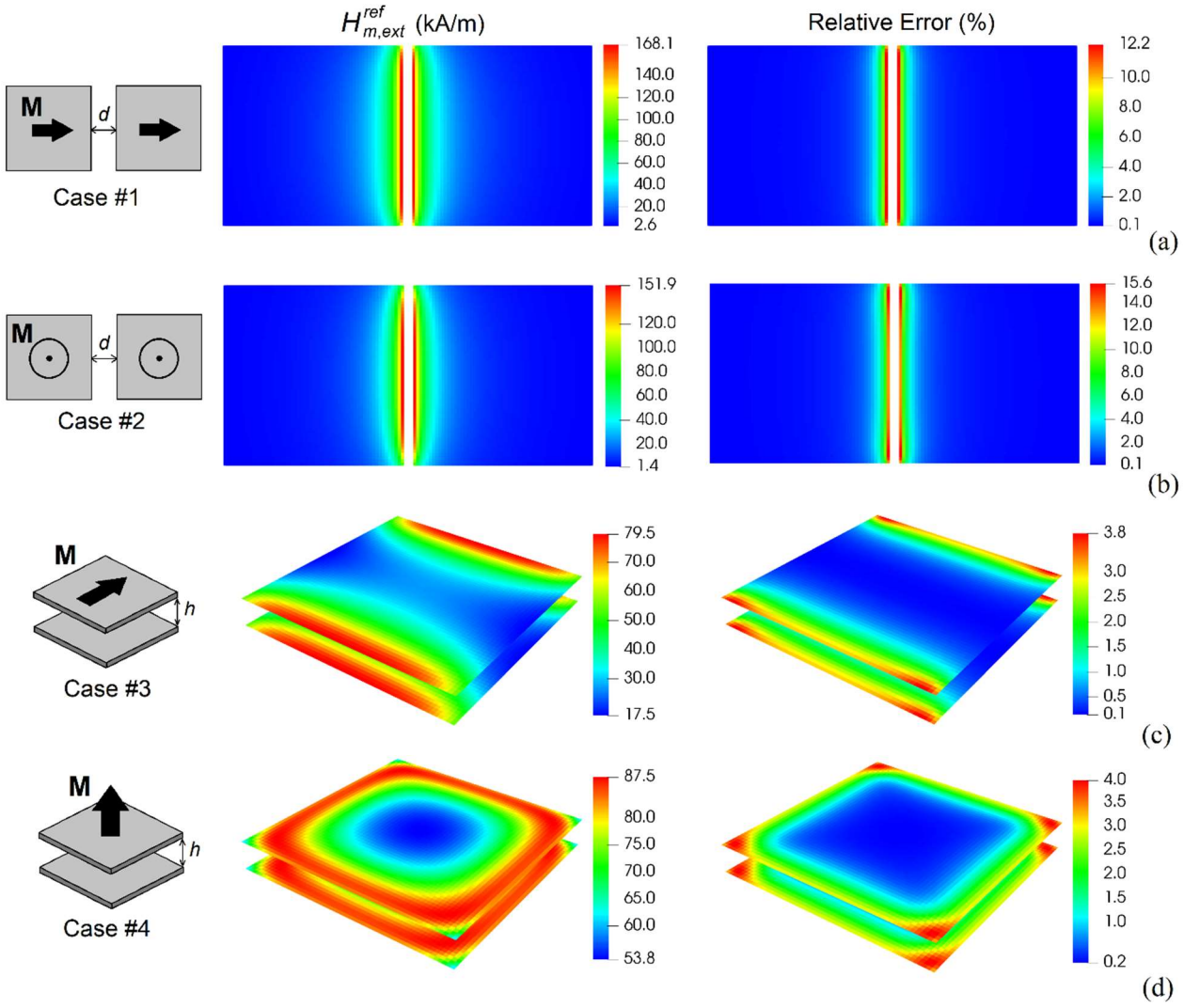

Fig. 2. On the left: schematics of the analysed cases with indication of the magnetization spatial distribution. In the centre: maps of the module of the external magnetostatic field term calculated by solving Green's integral equation (reference solution). On the right: maps of the relative error of the external magnetostatic field, obtained by approximating each object as a collection of magnetic dipoles. In the reported results parameters *d* and *h* are fixed to 10 nm.

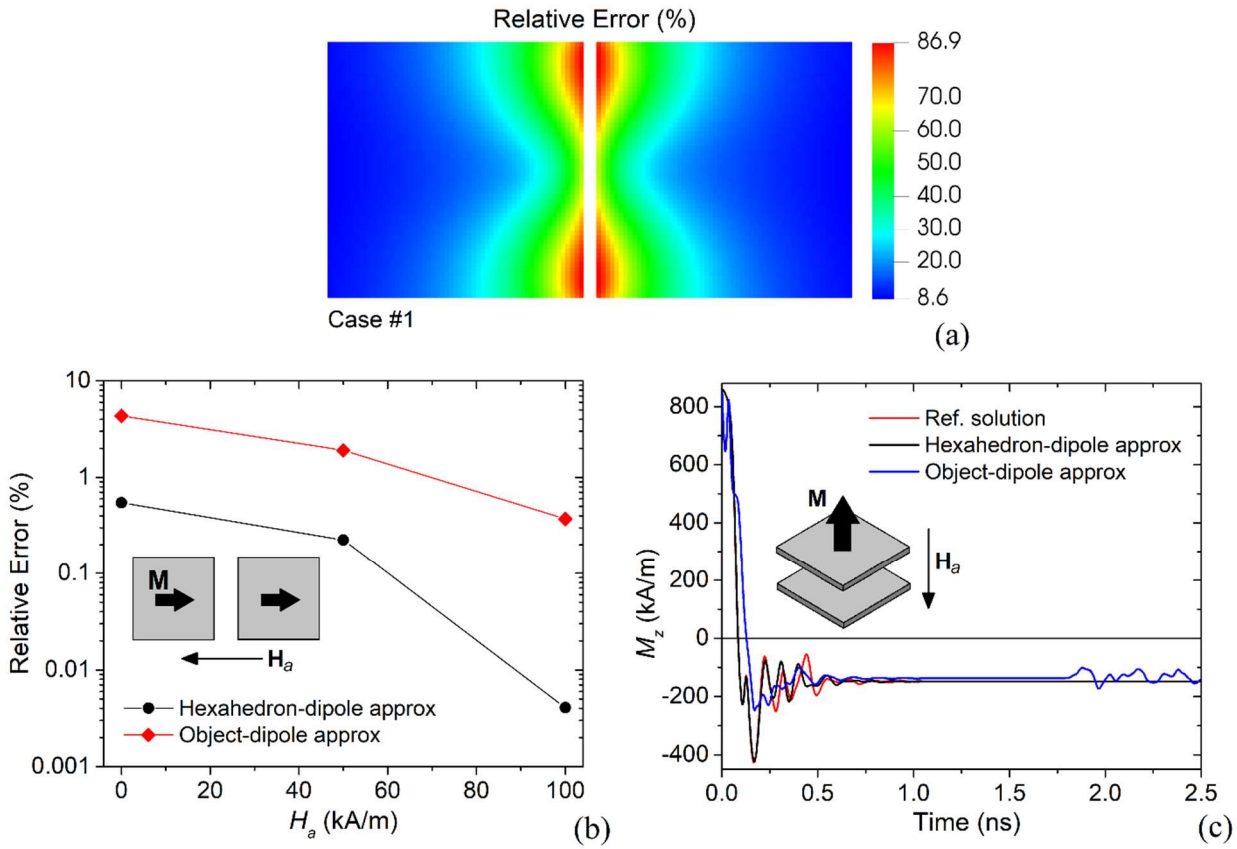

Fig. 3. (a) Map of the relative error of the external magnetostatic field, obtained for case #1 and d = 10 nm by approximating each object as a single magnetic dipole, centred in the object barycentre. The insets in (b) and (c) show the geometrical configuration, the initial uniform magnetization state and the direction of the external field. (b) Relative error in the average value of the x-component of the magnetization at the equilibrium state reached after the application of a uniform dc field (along negative x-axis) with variable amplitude H_a. The solutions are calculated with the hexahedron-dipole and object-dipole approximations, for d = 10 nm. (c) Time evolution of the z-component of the magnetization in presence of a uniform dc field with H_a = 100 kA/m, applied along negative z-axis. The solutions calculated for h = 10 nm with the hexahedron-dipole and object-dipole approximations are compared to the reference one, obtained via Green integral evaluation.

3.2 Analysis of computation time

We here investigate the computational cost of the developed 2.5D solver, highlighting its advantages when compared to a standard approach, where all the magnetostatic interactions are calculated via Green integration. The study is performed on a variable number N of objects, discretized with a fixed mesh composed of 1000 hexahedra. The algorithm can be split in two main blocks, a preliminary one,

where the local time-invariant system matrices **G** and **K*** are calculated and permanently transferred to GPU, and a second one, where the LLG equation is solved at each time instant.

The computation time for the first block, which involves the determination of the exchange and internal magnetostatic field matrices in the local reference frame (equal for each object), does not depend on N, but only on the number T of hexahedra. The assembly of the exchange field matrix **K*** requires a negligible computation time, 5000 times smaller than the one necessary to build the Green tensor **G** for the internal magnetostatic field term.

The non-dependence on N represents a great advantage in terms of computational efficiency and memory requirement. If we consider a standard approach, where the entire Green tensor is calculated at the beginning, we have to evaluate a total of $9N^2 \times T^2$ matrix elements, compared to a number of $9T^2$ elements for the developed 2.5D algorithm. This poses limits to the maximum number of objects that can be handled with a standard approach, e.g. with a GPU card NVIDIA Quadro K6000 we can treat up to 15 objects, considering the additional storage of the exchange field matrix. In this case, the total time to assemble the entire Green tensor is roughly 200 times larger than the one required for the matrix for the only internal magnetostatic field term.

The computation time for the second block is analysed in Fig. 4, which shows the time used for the calculation of the exchange field and of the internal and external magnetostatic field terms and for the update of the magnetization per each time instant. The computation time contributions, normalized to the time needed to calculate the external magnetostatic field with $N = 5$, are registered under the condition of optimal data transfer to GPU.

The most time-consuming task is the evaluation of the external magnetostatic field term $\mathbf{H}_{m,ext}$, which is directly computed in the absolute reference frame. For each of the $N \times T$ mesh elements (hexahedra), this consists in summing the dipole contributions from all the mesh elements belonging to the other (N-1) objects. As demonstrated by Fig. 4, the computation time of this operation is a quadratic function of N. A similar computation time is obtained with the standard approach (non-approximated calculation of $\mathbf{H}_{m,ext}$), up to the admissible number of objects (N = 15), since the geometric contributions have been already computed and stored in the preliminary part of the algorithm. With the used hexahedron-dipole approximation, described by (3), we can operate entirely in the GPU with a much larger number of objects (up to 95 with one NVIDIA Quadro K6000), without incurring in the bottleneck of the data transfer bandwidth between CPU and GPU.

A strong reduction in the computational cost of the inter-object magnetostatic interaction can be obtained by approximating the contribution from each object as the stray field of a single dipole, as described by (22). The reason is that in this case for each of the $N \times T$ mesh elements (hexahedra) we have to sum only (N-1) contributes. This effectively improves the scaling, which passes from $O(N^2T^2)$

to O(N^2T), but as shown in the previous Subsection the introduced approximation is not acceptable in terms of accuracy.

Concerning the computation of the internal magnetostatic field term $\mathbf{H}_{m,int}$ and of the exchange field $\mathbf{H}_{ex}$, which is performed in the local reference frame, we find a linear scaling with N. The operation of rotation of the fields from the local to the absolute reference frames concurs with a marginal cost. Finally, we analyse the computation time necessary to calculate the effective field in the absolute reference frame (sum of the different field contributions) and to update the magnetization according to the Cayley transform based scheme. A quadratic dependence on N is found; this time is negligible for low numbers of objects, becoming comparable to the one required for calculating the exchange and the internal magnetostatic fields for $N > 50$.

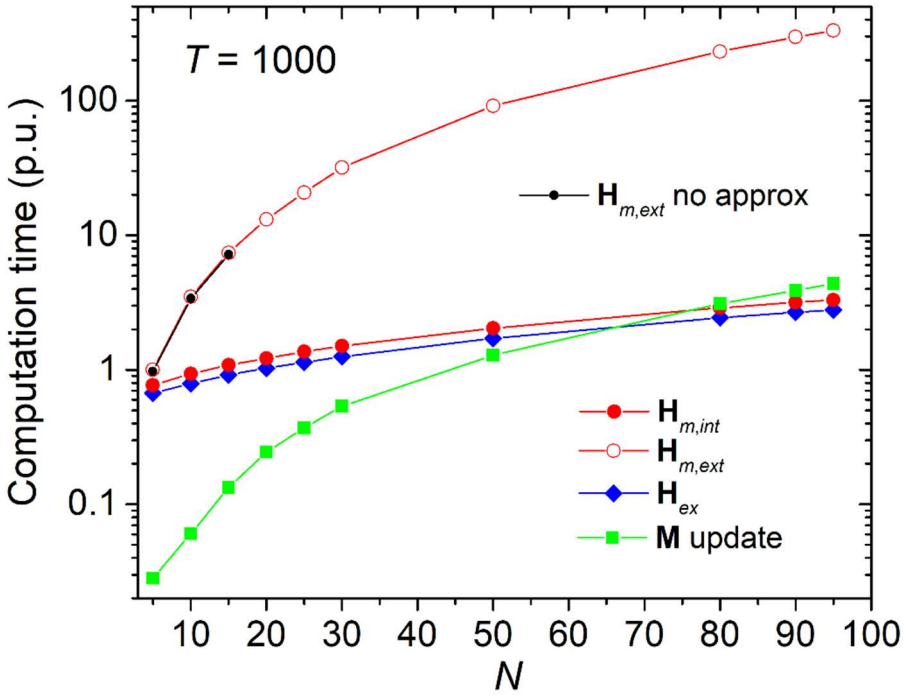

Fig. 4. Analysis of the computation time for distributions of N objects (discretized with 1000 hexahedra), separately considering the calculation of the exchange field and of the internal and external magnetostatic field terms and the update of magnetization at each time instant. The time required for the evaluation of the external magnetostatic field term without approximation is also reported for comparison, up to $N = 15$. The computation time contributions are normalized to the time needed to calculate the approximated external magnetostatic field with $N = 5$.

3.3. Application to 3D distributions of objects

In this Subsection we apply the 2.5D micromagnetic solver to calculate the hysteresis loops of ensembles of magnetic thin objects distributed in a 3D medium. The considered objects are circular nanodots made of permalloy, with diameter of 200 nm and thickness of 20 nm. For these samples, it is expected that the magnetization reversal process occurs via the nucleation, transverse motion and expulsion of a vortex [40].

As a first test, we consider a set of nanodots with the same orientation in the space, assuming that they lie parallel to the *xy*-plane of the absolute reference frame. In this case, it is possible to compare the solution calculated with the 2.5D solver with the one obtained with a 3D-FFT code. In the latter the magnetostatic field is computed by using an analytical expression for the demagnetizing tensor [41] and an FFT approach based on the discrete convolution theorem [42], and the exchange field is determined with a standard finite difference method. The application of the 3D-FFT code, which implements the same time-integration scheme of the 2.5D solver, requires the use of a structured mesh and the discretization of the volume containing all the objects. The 2.5D solver is more flexible, needing as an input the mesh of a single nanodot, which is non-structured to accurately reproduce the dot curved boundaries and thus avoid the introduction of fictitious shape anisotropy effects. The solutions are obtained by setting the damping coefficient α at 0.1, the parameter σ in (12) at 5γ and the time step at 1 ps, according to the analysis reported in Ref. [38]. The convergence to equilibrium points is verified when the maximum value of the local misalignment between magnetization and effective field, $\left|\mathbf{M}(\mathbf{r})\times\mathbf{H}_{eff}(\mathbf{r})\right| / M_S^2(\mathbf{r})$, is lower than a predetermined threshold, fixed to 10^{-8}.

Figure 5(a) shows the hysteresis loops of a distribution of 30 nanodots with a volume concentration of 25% (see inset), comparing the results obtained with the 2.5D and the 3D-FFT solvers. The volume concentration is defined as the ratio V_{dots}/V_{system}, where V_{dots} is the volume of a nanodot multiplied by the number of nanodots and V_{system} is the minimum volume of the 3D domain containing all the nanodots. The 2.5D code solution is calculated with a spatial discretization size Δs of 6.25 nm in the film plane, while the 3D-FFT code one is determined on a $0.8\times0.8\times0.16$ μm^3 volume, by fixing Δs to 6.25 nm along *x*- and *y*-axes and to 5 nm along *z*-axis. Figure 5(b) compares the different solvers in the computation of the specific magnetostatic energy for the entire ensemble of nanodots and for a single nanodot, coloured in black in the distribution in the inset of Fig. 5(a).

Overall, a good agreement is reached between the results obtained with the 2.5D and the 3D-FFT solvers. The small discrepancies are mainly attributable, for the 2.5D code, to the approximation of the interdot magnetostatic interactions and, for the 3D-FFT code, to the staircase reconstruction of the dot circular edges. The latter is responsible for the introduction of shape anisotropies and consequent pinning sites for the nucleation of vortexes. As a test, we calculate the spatial distribution

of the magnetostatic field $\mathbf{H}_m$ for two in-plane nanodots separated by a distance of 10 nm and magnetically saturated along x-axis. The solutions, reported in Fig. 6(a), are determined with both the 2.5D and 3D-FFT solvers and compared to the one obtained with the 2.5D code without the introduction of approximations in the evaluation of the external magnetostatic field (reference solution). The use of a structured mesh, imposed by the FFT technique, gives rise to strong discontinuities at the dot edges, resulting in differences between the spatial distributions of $\mathbf{H}_m$ calculated with the 2.5D and 3D-FFT solvers. These discrepancies can lead to a non-synchronous field-evolution of the magnetization inside the dots, as demonstrated by the comparison of the maps in Figs. 6(b), 6(c) and 6(d), which show the magnetization configurations at different equilibrium points along the descending branch of the hysteresis loops, for H_a equal to 20 kA/m (b), zero (c) and –50 kA/m (d). At the beginning of the reversal process, the maps calculated with the 2.5D and the 3D-FFT codes are very similar; at remanence, deviations appear for certain dots, due to variations in the computation of the external magnetostatic field term and in the dot mesh. As a consequence, the reversal mechanism of some dots could be different, with possible non-occurrence of vortex state. Despite the local differences in the equilibrium magnetization configurations, the 2.5D and 3D-FFT solvers are in good agreement in predicting the global behaviour of the ensemble of nanodots, as confirmed by the small discrepancies found in the hysteresis loop and magnetostatic energy of the entire system (Fig. 5). When moving from local to global behaviour, the differences reduce due to the averaging process. Indeed, almost all the dots are characterized by a vortex-based magnetization reversal; globally, vortex nucleation and expulsion fields are distributed over large field intervals, which can overlap when passing from a dot to another one. The non-synchronous magnetization switching due to the magnetostatic interactions between nanodots leads to a smooth global hysteresis loop with a succession of small irreversible jumps, easier to reproduce than the steep transitions occurring in each separated dot.

The computational performances of the 2.5D and 3D-FFT codes in calculating the instantaneous value of the magnetostatic field $\mathbf{H}_m$ are compared in Fig. 7 for the first test problem. Specifically, in Fig. 7(a) we report the time $\tau_{\mathbf{H}_m,\text{3D-FFT}}$ required by the 3D-FFT solver to update $\mathbf{H}_m$, as a function of the size of the computation volume $V_{computation}$. $\tau_{\mathbf{H}_m,\text{3D-FFT}}$ is normalized to the time necessary for the 2.5D code to calculate $\mathbf{H}_m$ when the number of nanodots N is equal to 30, considering that the computation cost of the 2.5D code is not affected by the size of the volume where the objects are distributed. On the contrary, the 3D-FFT code requires the discretization of the surrounding non-magnetic regions, with a consequent increase in the number of finite difference (FD) cells for low concentrations of objects. For the used spatial discretization (specified above) and for N = 30, the 2.5D code results more efficient than the 3D-FFT solver for computation volumes at least 4 times

larger than the one depicted in Fig. 5(a) ($0.8\times0.8\times0.16$ μm^3), assumed as a reference. The advantages of the 2.5D code become evident for great computation volumes, e.g. for an occupied volume 20 times bigger than the reference one the computation time is a seventh of the one of the 3D-FFT code, which requires more than 10^7 FD cells for the FFT evaluation.

In Fig. 7(b) we report the time for computing $\mathbf{H}_m$ via the 2.5D solver ($\tau_{\mathbf{H}_m,2.5\mathrm{D}}$), versus the number of nanodots N; the analysis is performed for two computation volumes (10 and 20 times larger than the reference one). $\tau_{\mathbf{H}_m,2.5\mathrm{D}}$ is normalized to the computation time required by the 3D-FFT solver, which is not affected by N, if the computation volume is fixed. It is interesting to note that for the larger volume the 2.5D solver is more efficient than the 3D-FFT one for $N \leq 75$, while for the smaller considered volume for $N \leq 55$.

In the previously analysed case, staircase reconstruction is imposed by the 3D-FFT code only to the dot circular edges, while dot faces are flat. Severe criticalities occur for random spatial distributions, where the thin-film objects can have different orientations with respect to the structured mesh axes. As described in Appendix A for a simple test case, when the objects are not aligned with the mesh grid, fictitious shape anisotropies are introduced due to the staircase reconstruction of faces. This leads to strong inaccuracies, which increase with the misalignment with respect to the mesh and can be reduced only by considering very small spatial discretization sizes.

In the following, we demonstrate the capability of the 2.5D code to reliably reproduce the behaviour of random distributions of thin-film objects. To test the accuracy, in Fig. 8(a) we compare the solutions obtained with the 2.5D solver, as described in Section 2, and without introducing approximations in the evaluation of the external magnetostatic field term. The analysis is performed by calculating the hysteresis loop of a distribution of 5 permalloy nanodots (diameter of 200 nm and thickness of 20 nm), differently oriented in the space and with a minimum (maximum) barycentre distance of 120 nm (300 nm). Very small differences are found, demonstrating the high-order approximation introduced by equation (3) and confirming the conclusions of Refs. [34, 35]. To test the efficiency of the 2.5D code, in the same figure we report the hysteresis loop calculated for a random distribution of 45 nanodots, with a volume concentration of 25%. Figure 8(b) reports the map of the relative magnetization configuration at remanence, well illustrating how the magnetostatic interactions and the different orientations with respect to the applied field lead to a non-synchronous evolution of the magnetization in the nanodots. As shown in Fig. 8(a), the increase in nanodot number leads to smoother hysteresis loops, with the disappearance of the steep jumps associated with vortex nucleation/expulsion transitions. In particular, vortexes are nucleated and expelled at different applied

fields, as a consequence of the magnetostatic interactions and of the variation in the angular orientation of nanodots with respect to the applied field [31].

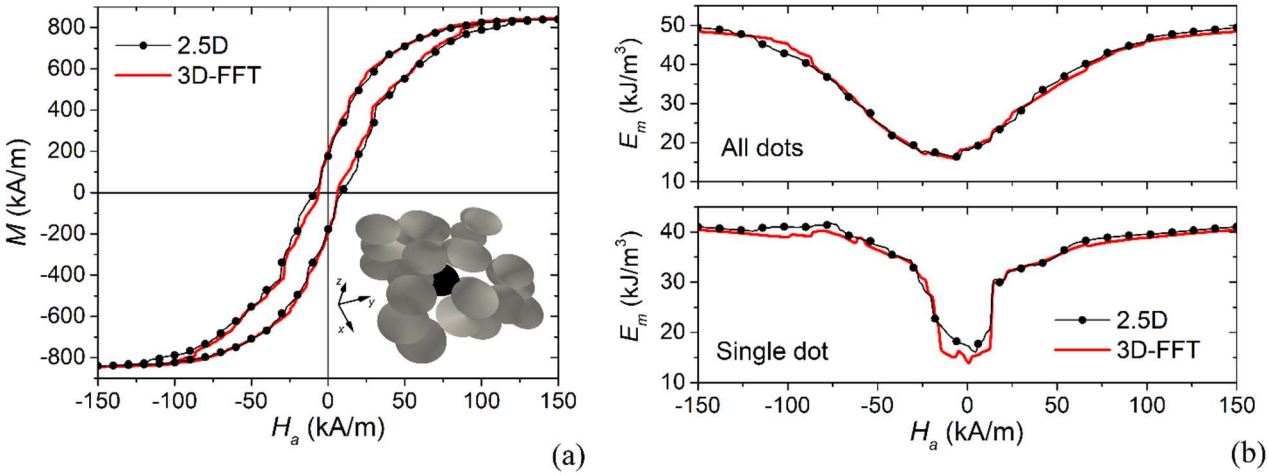

Fig. 5. (a) Comparison of the hysteresis loops calculated with the 2.5D and the 3D-FFT solvers, in the case of a distribution of 30 permalloy nanodots lying parallel to the *xy*-plane of the absolute reference frame (inset). The nanodot diameter is 200 nm and the thickness is 20 nm; the external field is applied along *x*-axis. (b) Comparison of the magnetostatic energy for the entire set of nanodots (top) and for a single nanodot (bottom), coloured in black in the distribution in the inset of (a).

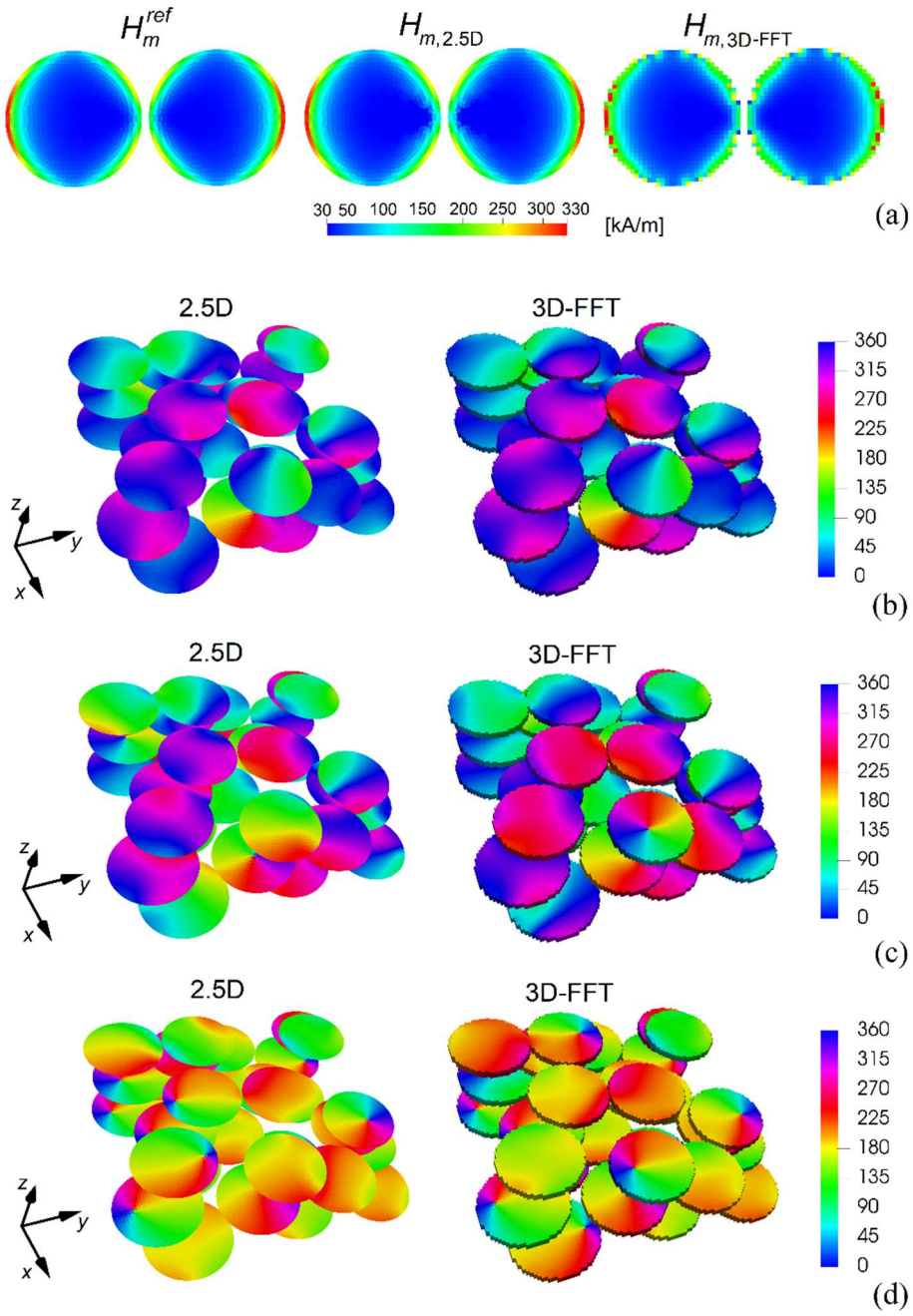

Fig. 6. (a) Spatial distributions of the module of the magnetostatic field for two in-plane nanodots separated by a distance of 10 nm and magnetically saturated along *x*-axis. The solutions are obtained with the 2.5D code without approximating the external magnetostatic field term (left), the 2.5D code (middle) and the 3D-FFT code (right). Magnetization configurations calculated with the 2.5D (left) and the 3D-FFT (right) solvers at different equilibrium points along the descending branch of the hysteresis loops in Fig. 5(a). The maps are reported for H_a equal to 20 kA/m (b), zero (c) and –50 kA/m (d), considering an external field applied along *x*-axis. The colour bar represents the angle, in degrees, between magnetization component in the *xy*-plane and *x*-axis.

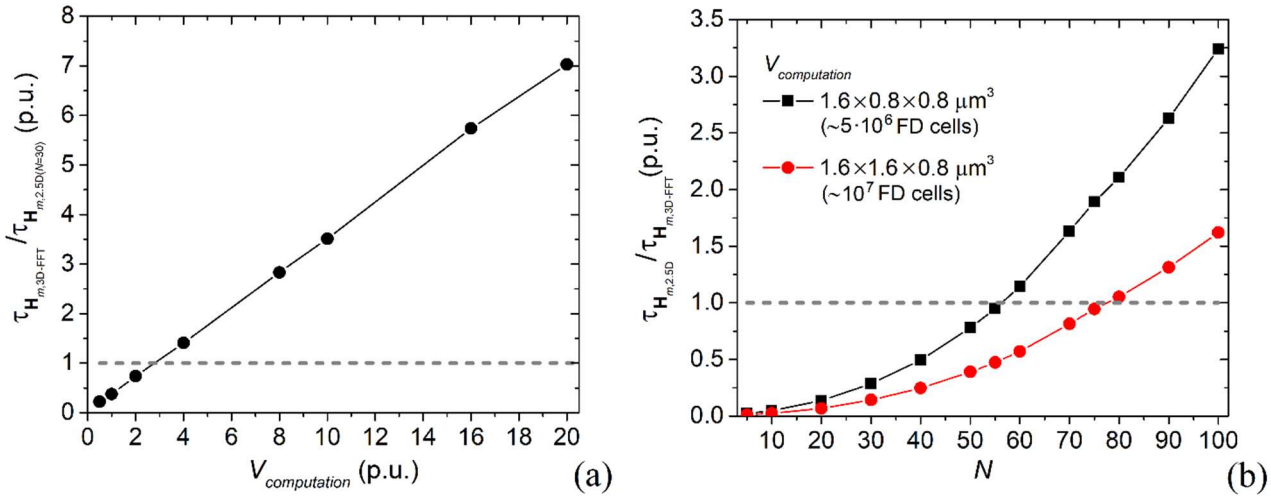

Fig. 7. (a) Computation time $\tau_{\mathbf{H}_{m,\text{3D-FFT}}}$ required by the 3D-FFT solver for the magnetostatic field update, versus the computation volume size (1 p.u. refers to 0.8×0.8×0.16 μm^3); $\tau_{\mathbf{H}_{m,\text{3D-FFT}}}$ is normalized to the time used by the 2.5D code when $N = 30$. (b) Computation time $\tau_{\mathbf{H}_{m,\text{2.5D}}}$ required by the 2.5D solver for the magnetostatic field update, as a function of N and for two computation volumes (10 and 20 times larger than the reference one); $\tau_{\mathbf{H}_{m,\text{2.5D}}}$ is normalized to the computation time used by the 3D-FFT solver.

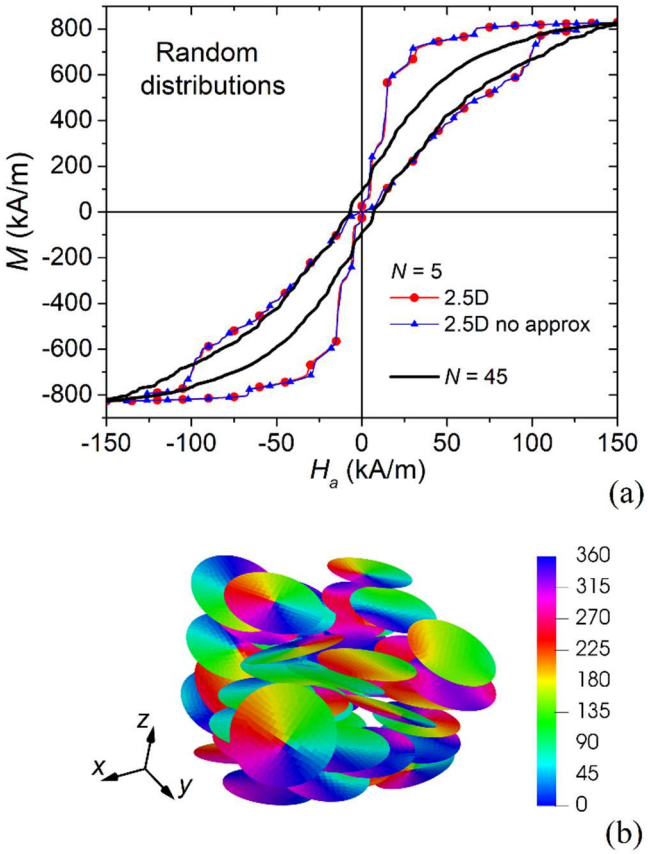

Fig. 8. (a) Hysteresis loops calculated with the 2.5D solver for two random distributions of permalloy nanodots, with N equal to 5 and 45. The solution obtained for $N = 5$ is compared to the one where the external magnetostatic field term is not approximated and is determined via Green integration. (b) Magnetization configuration calculated at remanent state for the case with $N = 45$. The colour bar represents the angle, in degrees, between magnetization component in the xy-plane and x-axis (direction of application of the external field).

4. Conclusions

We have developed a GPU-parallelized 2.5D micromagnetic solver that is able to efficiently simulate the magnetization dynamics in 3D distributions of magnetic thin-film objects, randomly arranged in a non-discretized space. Thanks to the integration of a finite difference method for the exchange field calculation on non-structured meshes, objects with complex shape can be easily handled, without the introduction of fictitious shape anisotropy effects. Moreover, the mesh element-dipole approximation introduced in the evaluation of the inter-object magnetostatic interactions permits to efficiently simulate large numbers of objects, with strong reductions in the computation time needed to assemble Green tensor as well as in memory requirements.

In the present study, the developed 2.5D solver has been successfully applied to calculate the hysteresis loop of a high number of strongly interacting magnetic circular nanodots, with different

orientations in the space and with respect to the applied field. The analysis has put in evidence the great advantages of the 2.5D code in comparison to standard 3D-FFT solvers, which are typically used for the simulation of large samples. In this case, the use of non-structured meshes does not allow to accurately treat problems with thin objects having complex shape and not aligned with mesh grid. Moreover, the need to discretize the non-magnetic medium surrounding the objects affects in a strong way the computational efficiency, while with the 2.5D solver the computational cost does not vary with the extension of the volume where the objects are distributed.

As an example, all the above features make the developed 2.5D code particularly suitable for the determination of the hysteresis losses of highly concentrated magnetic nanosystems (e.g. nanodisks, nanorings), recently proposed as novel heat mediators for magnetic hyperthermia applications.

As further developments, the 2.5D solver can be generalized to enable the handling of different types of objects, with variable size and shape. In this case, the preliminary block of the algorithm would involve the calculation of more time-invariant matrices for the internal magnetostatic field term and the exchange field, one for each type of object.

Acknowledgments

The authors are grateful to Dr. Oriano Bottauscio (INRIM) for the help in the GPU-parallelization of the 2.5D micromagnetic code.

Appendix A

We here show how strong inaccuracies arise when applying 3D-FFT micromagnetic codes to the solution of even simple problems, where structured meshes do not appropriately reproduce the object shape (e.g. for objects not aligned with mesh grid). As an example, we calculate the hysteresis loop of a thin permalloy square (200 nm size and 15 nm thickness) for two equivalent configurations in terms of object-applied field orientation. The two considered cases are illustrated in the schematic of Fig. A.1. Given a common absolute reference frame (x, y, z), in case #1 the film is oriented parallel to the xy-plane and the external field is applied along a direction that forms an angle of 45° with the x-axis, namely $\mathbf{H}_a = H_a\left(\sqrt{2}/2, 0, \sqrt{2}/2\right)$. In case #2, the film is inclined of 45° with respect to the xy-plane and the external field is aligned with the x-axis.

Figure A.2 reports the hysteresis loops for the two analysed cases, calculated with the 2.5D solver as well as with the 3D-FFT code employed in the tests of Subsection 3.3. Even if from physical and geometrical point of view the two problems are equivalent, very different results are obtained with the 3D-FFT code when adopting, for both cases, a mesh aligned with the reference frame (x, y, z). The reason is that in case #2 the use of 3D-FFT code forces to reconstruct the object edges and faces with a staircase function, introducing fictitious shape anisotropy effects. As a consequence, for a spatial discretization Δs of 5 nm (see the bottom of Fig. A.1), strong discrepancies are found between the solutions of problems #1 and #2 computed with the 3D-FFT code. On the contrary, the two solutions are identical when using the 2.5D solver, since the same discretization mesh is employed, apart from a rotation with respect to the reference frame. As expected, these solutions practically coincide with the one of problem #1 calculated with the 3D-FFT code.

Finally, it is interesting to note that with a finer mesh (Δs = 2.5 nm) the solution of problem #2 calculated with the 3D-FFT code is a bit closer to the other three ones, but strong discrepancy remains. Moreover, the computational cost rises dramatically, due to the increase in the FFT matrix size (including the contributions also from non-magnetic FD cells) and the simultaneous reduction in the time step that guarantees numerical stability. For a single object, these criticalities can be avoided by generating a mesh aligned with the object itself. However, these strong limitations of 3D-FFT solvers cannot be bypassed when one has to handle multiple objects, like thin films, with different spatial orientations in a 3D medium.

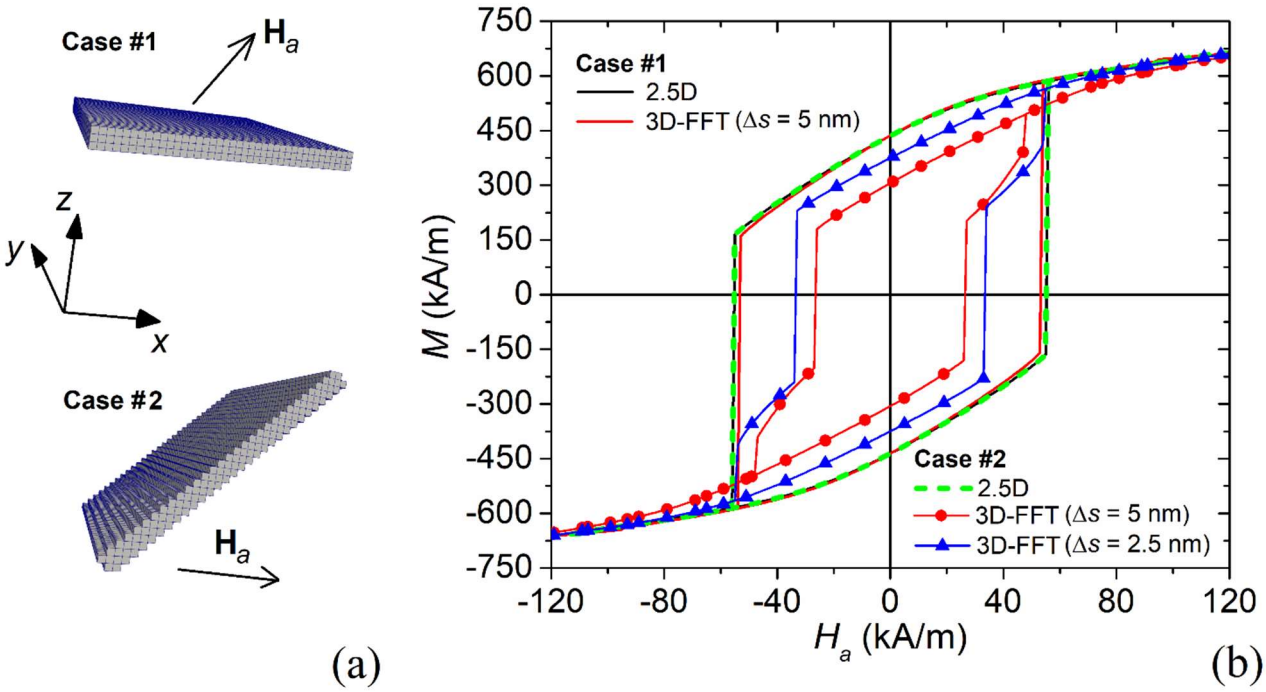

Fig. A.1. (a) Schematics of the two considered cases with a permalloy thin film (size of 200 nm and thickness of 15 nm) inclined of 45° with respect to the applied field $\mathbf{H}_a$. (b) Hysteresis loops for the two cases calculated with both the 2.5D solver and a 3D-FFT code that uses a structured mesh aligned with the reference frame (x, y, z). The 2.5D code solutions are calculated with a spatial discretization size Δs of 5 nm in the film plane, while the 3D-FFT code ones by fixing Δs to 5 nm (as shown in the schematics) and to 2.5 nm.

References

[1] B. Van de Wiele, F. Olyslager, L. Dupré, Application of the fast multipole method for the evaluation of magnetostatic fields in micromagnetic computations, J. Comput. Phys. 227 (23) (2008) 9913-9932.

[2] Y. Takahashi, S. Wakao, T. Iwashita, M. Kanazawa, Micromagnetic simulation by using the fast multipole method specialized for uniform brick elements, J. Appl. Phys. 105 (7) (2009) 07D514.

[3] D. M. Apalkov, P. B. Visscher, Fast multipole method for micromagnetic simulation of periodic systems, IEEE Trans. Magn. 39 (6) (2003) 3478-3480.

[4] C. Seberino, H. N. Bertram, Concise, efficient three-dimensional fast multipole method for micromagnetics, IEEE Trans. Magn. 37 (3) (2001) 1078-1086.

[5] P. Palmesi, L. Exl, F. Bruckner, C. Abert, D. Suess, Highly parallel demagnetization field calculation using the fast multipole method on tetrahedral meshes with continuous sources, J. Magn. Magn. Mat. 442 (2017) 409-416.

[6] A. Manzin, O. Bottauscio, Multipole expansion technique for the magnetostatic field computation in patterned magnetic films, J. Appl. Phys. 111 (7) (2012) 07D125.

[7] A. Manzin, O. Bottauscio, A Micromagnetic Solver for Large-Scale Patterned Media Based on Non-Structured Meshing, IEEE Trans. Magn. 48 (11) (2012) 2789-2792.

[8] A. Vansteenkiste, J. Leliaert, M. Dvornik, M. Helsen, F. Garcia-Sanchez, B. Van Waeyenberge, The design and verification of MuMax3, AIP Advances 4 (10) (2014) 107133.

[9] L. Exl, T. Schrefl, Non-uniform FFT for the finite element computation of the micromagnetic scalar potential, J. Comput. Phys. 270 (2014) 490-505.

[10] H. H. Long, E. T. Ong, Z. J. Liu, E. P. Li, Fast Fourier Transform on Multipoles for Rapid Calculation of Magnetostatic Fields, IEEE Trans. Magn. 42 (2) (2006) 295-300.

[11] Z. J. Liu, H. H. Long, E. T. Ong, E. P. Li, A fast Fourier transform on multipole algorithm for micromagnetic modeling of perpendicular recording media, J. Appl. Phys. 99 (8) (2006) 08B903.

[12] C. Abert, L. Exl, G. Selke, A. Drews, T. Schrefl, Numerical methods for the stray field calculation: a comparison of recently developed algorithms, J. Magn. Magn. Mat. 326 (2013) 176-185.

[13] C. Abert, L. Exl, F. Bruckner, A. Drews, D. Suess, magnum.fe: A micromagnetic finite-element simulation code based on FEniCS, J. Magn. Magn. Mat. 345 (2013) 29-35.

[14] R. Hertel, S. Christophersen, S. Börm, Large-scale magnetostatic field calculation in finite element micromagnetics with H^2-matrices, J. Magn. Magn. Mat. 477 (1) (2019) 118-123.

[15] F. Bruckner, C. Vogler, M. Feischl, D. Praetorius, B. Bergmair, T. Huber, M. Fuger, D. Suess, 3D FEM–BEM-coupling method to solve magnetostatic Maxwell equations, J. Magn. Magn. Mat. 324 (10) (2012) 1862-1866.

[16] O. Bottauscio, M. Chiampi, A. Manzin, A Finite Element Procedure for Dynamic Micromagnetic Computations, IEEE Trans. Magn. 44 (11) (2008) 3149-3152.

[17] M. J. Donahue, Parallelizing a Micromagnetic Program for Use on Multiprocessor Shared Memory Computers, IEEE Trans. Magn. 45 (10) (2009) 3923-3925.

[18] S. Li, B. Livshitz, V. Lomakin, Graphics Processing Unit Accelerated O(N) Micromagnetic Solver, IEEE Trans. Magn. 46 (6) (2010) 2373-2375.

[19] O. Bottauscio, A. Manzin, Parallelized micromagnetic solver for the efficient simulation of large patterned magnetic nanostructures, J. Appl. Phys. 115 (17) (2014) 17D122.

[20] A. Kakay, E. Westphal, R. Hertel, Speedup of FEM Micromagnetic Simulations With Graphical Processing Units, IEEE Trans. Magn. 46 (6) (2010) 2303-2306.

[21] J. Leliaert, M. Dvornik, J. Mulkers, J. De Clercq, M. V. Milošević, B. Van Waeyenberge, Fast micromagnetic simulations on GPU - recent advances made with mumax^3, J. Phys. D: Appl. Phys. 51 (12) (2018) 123002.

[22] L. Lopez-Diaz, D. Aurelio, L. Torres, E. Martinez, M. A. Hernandez-Lopez, J. Gomez, O. Alejos, M. Carpentieri, G. Finocchio, G. Consolo, Micromagnetic simulations using Graphics Processing Units, J. Phys. D: Appl. Phys. 45 (32) (2012) 323001.

[23] S. Fu, W. Cui, M. Hu, R. Chang, M. J. Donahue, V. Lomakin, Finite-Difference Micromagnetic Solvers With the Object-Oriented Micromagnetic Framework on Graphics Processing Units, IEEE Trans. Magn. 52 (4) (2016) 7100109.

[24] G. Barrera, F. Celegato, M. Coïsson, A. Manzin, F. Ferrarese Lupi, G. Seguini, L. Boarino, G. Aprile, M. Perego, P. Tiberto, Magnetization switching in high-density magnetic nanodots by a fine-tune sputtering process on a large-area diblock copolymer mask, Nanoscale 9 (43) (2017) 16981-16992.

[25] S. Louis, I. Lisenkov, S. Nikitov, V. Tyberkevych, A. Slavin, Bias-free spin-wave phase shifter for magnonic logic, AIP Advances 6 (2016) 065103.

[26] A. Manzin, G. Barrera, F. Celegato, M. Coïsson, P. Tiberto, Influence of lattice defects on the ferromagnetic resonance behaviour of 2D magnonic crystals, Scientific Reports 6 (2016) 22004.

[27] M. Sushruth, J. Ding, J. Duczynski, R. C. Woodward, R. A. Begley, H. Fangohr, R. O. Fuller, A. O. Adeyeye, M. Kostylev, P. J. Metaxas, Resonance-based detection of magnetic nanoparticles and microbeads using nanopatterned ferromagnets, Phys. Rev. Applied 6 (2016) 044005.

[28] Y.-L. Wang, Z.-L. Xiao, A. Snezhko, J. Xu, L. E. Ocola, R. Divan, J. E. Pearson, G. W. Crabtree, W.-K. Kwok, Rewritable artificial magnetic charge ice, Science 352 (6288) (2016) 962-966.
[29] Y. Yang, X. Liu, Y. Lv, T. S. Herng, X. Xu, W. Xia, T. Zhang, J. Fang, W. Xiao, J. Ding, Orientation Mediated Enhancement on Magnetic Hyperthermia of Fe_3O_4 Nanodisc, Advanced Functional Materials 25 (5) (2015) 812-820.
[30] K. Simeonidis, M. Puerto Morales, M. Marciello, M. Angelakeris, P. de la Presa, A. Lazaro-Carrillo, A. Tabero, A. Villanueva, O. Chubykalo-Fesenko, D. Serantes, In-situ particles reorientation during magnetic hyperthermia application: Shape matters twice, Scientific Reports 6 (2016) 38382.
[31] R. Ferrero, A. Manzin, G. Barrera, F. Celegato, M. Coïsson, P. Tiberto, Influence of shape, size and magnetostatic interactions on the hyperthermia properties of permalloy nanostructures, Scientific Reports 9 (2019) 6591.
[32] O. Bottauscio, A. Manzin, Spatial reconstruction of exchange field interactions with a Finite Difference scheme based on unstructured meshes, IEEE Trans. Magn. 48 (11) (2012) 3250-3253.
[33] T.Liszka, J.Orkisz, The finite difference method at arbitrary irregular grids and its application in applied mechanics, Computers & Structures 11 (1–2) (1980) 83-95.
[34] J. H. J. van Opheusden, E. M. C. M. Reuvekamp, Computer simulation of a thin magnetic film with vertical anisotropy, J. Magn. Magn. Mat. 88 (1–2) (1990) 247-259.
[35] E. D. Boerner, H. N. Bertram, Dynamics of thermally activated reversal in nonuniformly magnetized single particles, IEEE Trans. Magn. 33 (5) (1997) 3052–3054.
[36] O. Bottauscio, A. Manzin, Efficiency of the geometric integration of Landau–Lifshitz–Gilbert equation based on Cayley transform, IEEE Trans. Magn. 47 (5) (2011) 1154-1157.
[37] D. Lewis, N. Nigam, Geometric integration on spheres and some interesting applications, J. Comput. Appl. Math. 151 (1) (2003) 141-170.
[38] A. Manzin, O. Bottauscio, Connections between numerical behavior and physical parameters in the micromagnetic computation of static hysteresis loops, J. Appl. Phys. 108 (9) (2010) 093917.
[39] E. Martínez, L. López-Díaz, L. Torres, C. J. García-Cervera, Minimizing cell size dependence in micromagnetics simulations with thermal noise, J. Phys. D: Appl. Phys. 40 (2007) 942-948.
[40] V. Novosad, K. Yu. Guslienko, H. Shima, Y. Otani, K. Fukamichi, N. Kikuchi, O. Kitakami, Y. Shimada, Nucleation and annihilation of magnetic vortices in sub-micron permalloy dots, IEEE Trans. Magn. 37 (4) (2001) 2088-2090.
[41] H. Fukushima, Y. Nakatani, N. Hayashi, Volume average demagnetizing tensor of rectangular prisms, IEEE Trans. Magn. 34 (1) (1998) 193-198.

[42] R. D. McMichael, M. J. Donahue, D. G. Porter, J. Eicke, Comparison of magnetostatic field calculation methods on 2-D square grids as applied to a micromagnetic standard problem, J. Appl. Phys. 85 (1999) 5816-5818.